Scaling of moored surface ocean turbulence measurements in the Southeast Pacific Ocean

Una Kim Miller[1], Christopher J. Zappa[1], Seth Zippel[2], J. Thomas Farrar[2], and Robert A. Weller[2]

[1]Lamont-Doherty Earth Observatory, Columbia University, Palisades, NY, USA

[2]Woods Hold Oceanographic Institution, Falmouth, MA, USA

Corresponding author: Una Miller (ukm2103@columbia.edu)

Key points

- Moored instrumentation allows for prolonged timeseries of turbulence estimates with concurrent in-situ meteorological and wave measurements

- Dissipation rate is scaled well by Law of the Wall in shear-dominant regimes and by surface buoyancy flux in convective-dominant regimes

- It is unnecessary in the Southeast Pacific Stratus region to distinguish between a wind-driven and Langmuir-driven turbulence regime

Abstract

Estimates of turbulence kinetic energy (TKE) dissipation rate (ε) are key to understanding how heat, gas, and other climate-relevant properties are transferred across the air-sea interface and mixed within the ocean. A relatively new method involving moored pulse-coherent Acoustic Doppler Current Profilers (ADCPs) allows for estimates of ε with concurrent surface flux and wave measurements across an extensive length of time and range of conditions. Here, we present 9 months of moored estimates of ε at a fixed depth of 8.4m at the Stratus mooring site (20°S, 85°W). We find that shear- and buoyancy-dominant turbulence regimes are defined equally well using the Obukhov length scale (L_M) and the newer Langmuir stability length scale (L_L), suggesting that ocean-side friction velocity (u_*) implicitly captures the influence of Langmuir circulation at this site. This is illustrated by a strong linear dependence between surface Stokes drift (u_s) and u_* and is likely facilitated by the steady Southeast trade winds regime. The traditional Law of the Wall (LOW) and surface buoyancy flux scalings of Monin-Obukhov similarity theory scale our estimates of ε well, collapsing data points near unity. We find that the newer Stokes drift scaling ($\frac{u_*^2 u_s}{mixed\ layer\ depth}$) scales ε well at times but is overall less consistent than LOW. Scaling relationships from prior studies in a variety of aquatic and atmospheric settings largely agree with our data in destabilizing, shear-dominant conditions but diverge in other regimes.

Plain Language Summary

Surface ocean turbulence is key in the transfer of heat, gas, and other climate-relevant properties between the ocean and atmosphere. Turbulence can be understood through estimates of turbulence kinetic energy (TKE) dissipation rate (ε), which is a measure of the rate of dissipation of turbulent energy into heat energy. Higher values of ε indicate a more turbulent environment. Because ε is important but difficult to estimate in the field, much effort has been put into parameterizing it from more easily obtainable variables such as wind speed, wave measurements, and surface buoyancy flux. Here, we test these parameterizations against an extensive timeseries of ε estimates collected on a mooring line attached to a surface buoy in the Southeast Pacific Ocean. This region is known to support important South American fisheries as well play a significant role in the global radiation budget, yet is poorly represented in climate models. We find the wind- and buoyancy flux-based parameterizations to describe our estimates of ε well, and we explore how conditions at the study site influence their performance.

1 Introduction

Turbulence kinetic energy (TKE) represents processes that drive the mixing of heat, momentum, and gas within and between the ocean and atmosphere, making it an important parameter in studies of weather and climate. It is generated in the Ocean Boundary Layer (OBL) primarily by wind- and wave-driven shear and buoyancy-driven convection, though wave breaking and other turbulent processes can play a significant role as well. Assuming a horizontally homogeneous flow, the TKE budget may be written as

$$\frac{D\bar{e}}{Dt} = -\underbrace{\overline{\boldsymbol{u}_h' w'} \cdot \frac{\partial \boldsymbol{u}_h}{\partial z}}_{\substack{Shear\\ production}} - \underbrace{\overline{\boldsymbol{u}_h' w'} \cdot \frac{\partial \boldsymbol{u}_s}{\partial z}}_{\substack{Stokes\\ production}} + \underbrace{\overline{w'B_0'}}_{\substack{Buoyant\ production/\\ destruction}} - \underbrace{\frac{\partial}{\partial z}\left(\overline{w'u_i'u_i{}'} + \frac{1}{\rho_0}(\overline{w'p'})\right)}_{Transport} - \underbrace{\varepsilon}_{\substack{Destruction\ by\ viscous\\ dissipation}} \qquad 1.$$

where e is TKE, $\boldsymbol{u_h}$ and w are horizontal and vertical velocities, $\boldsymbol{u_s}$ is the Stokes drift velocity vector, B_0 is surface buoyancy flux, ρ_0 is background density, and p is pressure. Prime notation indicates the turbulent component of a Reynolds decomposed quantity, overbars indicate a time mean, and the subscript i indicates tensor notation. The shear production term describes TKE from the shear of currents generated by winds at the surface while the Stokes production term describes that of the shear of Stokes drift associated with surface waves. The interaction of Stokes drift with the shear of the wind-driven current results in Langmuir circulation, characterized by vertically-oriented, counter-rotating vortices that are often visible at the surface as streaks of foam or kelp aligned in the direction of the wind (Craik and Leibovich, 1976). These vortices result in enhanced turbulent vertical velocities that aid in the transport of TKE generated near the surface to the base of the mixed layer (e.g. Sutherland et al., 2014), via the turbulent transport term. This plays an important role in the deepening of the mixed layer (Belcher et al., 2012; Li and Fox-Kemper, 2017). The buoyancy term describes the production of TKE by free convection associated with destabilizing surface buoyancy fluxes or its destruction by stratification caused by stabilizing fluxes.

The rate of TKE dissipation (ε) into heat is of particular interest because it must, on average, equal the total TKE generated in a system. Traditional parameterizations of ε assume a simplified version of Equation 1 in which the production of TKE by current shear or convection is balanced by its dissipation. In the absence of surface waves (i.e., the OBL is a “wall”-bounded layer) and buoyancy flux, the wind term may be scaled using friction velocity (u_*) to give rise to the Law of the Wall (LOW),

$$\varepsilon \sim u_*^3/\kappa|z| \qquad 2.$$

where the von Kármán constant, κ, is 0.4. Likewise in the absence of waves and wind, ε scales with surface buoyancy flux (B_0):

$$\varepsilon \sim B_0 \qquad 3.$$

Early studies of the application of LOW and Equation 3 in the OBL include Shay and Greg (1986), Anis and Moum (1992) and Brainerd and Gregg (1993). Dimensional analysis of LOW and Equation 3 gives rise to a key length scale known as the Obukhov length scale,

$$L_M = \frac{-u_*^3}{\kappa B_0} \qquad 4.$$

which may be conceptualized as the depth at which buoyancy and mechanical shear contribute equally to turbulence in the ocean (e.g. Stull, 1988). It follows that buoyancy forcing dominates the TKE regime where $\left|\frac{z}{L_M}\right| > 1$ (production in convective conditions, suppression in stable conditions) and wind forcing dominates where $\left|\frac{z}{L_M}\right| < 1$. This serves as the basis for scaling relationships derived from Monin-Obukhov (MO) similarity theory (Monin and Obukhov, 1959).

In the atmosphere, MO scaling relationships for ε typically take the form of

$$\frac{\varepsilon\kappa z}{u_*^3} = \left[A^{1/M_1} + B^{1/M_2}|z/L_M|^{1/M_3}\right]^{M_4} \quad 5.$$

where A, B, and M_i are empirically derived coefficients and z is height. Here, ε is nondimensionalized by LOW. In the OBL, this equation is often rearranged by dividing through by LOW and setting M equal to unity such that ε is presented as a linear combination of TKE production by wind and buoyant forcing:

$$\varepsilon = A\frac{u_*^3}{\kappa z} + BB_0 \quad 6.$$

where A and B are typically determined by the averages of $\varepsilon/\frac{u_*^3}{\kappa z}$, and ε/B_0 in their respective dominant regimes, and B_0 is restricted to positive values (turbulence producing rather than suppressing). Equation 6 was first proposed in Lombardo and Gregg (1989) for an intermediate L_M-defined regime in which both mechanical and buoyant forcing contributed significantly to turbulence production, though they found it also scaled measurements of turbulence fairly well across all observed conditions.

The representation of the OBL in MO Similarity Theory as a wave-free, wall-bounded layer has been challenged by decades of observational studies of turbulence generated by surface wave breaking (Agrawal et al., 1992; Anis and Moum, 1995; Craig and Banner, 1994; Drennan et al., 1992; Gemmrich and Farmer, 2004; Soloviev and Lukas, 2003; Terray et al., 1996) and wind-wave interaction (D'Asaro, 2014; Sutherland et al., 2014). Wave breaking directly injects turbulence into the near-surface "breaking layer", which extends down to a depth of approximately 0.6 the significant wave height (H_{sw}) (Gerbi et al., 2009; Terray et al., 1996). TKE generated in this layer is transported downwards to a "transition layer", also known as wave-affected surface layer (WASL) (Gerbi et al., 2009; Stips et al., 2005). According to Terray et al., (1996), this transition layer is bounded below by the transition depth, z_t, though observational studies have since shown mixed results on its presence or extent (Esters et al., 2018; Sutherland and Melville, 2015). Dissipation rates are expected to deviate from MO Similarity Theory (Equations 2, 3, 5, and 6) in the breaking and transition layers, and conform below, where TKE from waves has dissipated entirely.

While TKE generated through surface wave breaking and the shear of Stokes drift velocities is largely confined to the upper few meters of the water column, Langmuir circulation can distribute turbulence to the base of the mixed layer through its associated enhancement of vertical transport. Because of its importance to mixed layer deepening, there have been many efforts to parameterize Langmuir circulation in models of the OBL (Li et al., 2019). The Langmuir number, $L_a = \sqrt{u_*/u_s}$, arises from a scaled ratio of the wind and wave terms in Equation 1 and describes the strength of Langmuir circulation (McWilliams et al., 1997). For well-developed seas, $L_a{\sim}0.4$ (Belcher et al., 2012; Sutherland et al., 2014), though misalignment of wind and waves is known to broaden the range of L_a (Van Roekel et al., 2012). According to LES results from Grant and Belcher (2009), a distinct Langmuir-driven regime is defined where

$L_a < 0.5$, with the transition to a wind-dominant regime occurring between $0.5 < L_a < 2$. A second term, the Langmuir stability length scale, $L_L = -u_*^2 u_s / B_0$, similarly arises from the scaled ratio of the wave and buoyancy terms in Equation 1. It describes the relative strength of Langmuir circulation to buoyant forcing (Belcher et al., 2012) and the use of $\frac{h}{L_L}$ to define turbulence regimes, where h is mixed layer depth, is analogous to that of z/L_M. Belcher et al. (2012) defines Langmuir-dominant and buoyancy-dominant regimes as $\frac{h}{L_L} > 1$ and $\frac{h}{L_L} < 1$, respectively, but because this term contains both u_s and u_*, it can also be considered a delineation of a buoyancy-dominant regime and that of a composite "wind-wave-induced" turbulence that includes the contributions of both wind-induced current shear and Langmuir circulation (Esters et al., 2018; Sutherland et al., 2014).

Because wind and waves are intrinsically tied, there is some question as to whether it is necessary to parameterize Langmuir circulation separately, or if the implicit incorporation of wave effects in traditional wind scaling parameterizations is sufficient. In their model study on the global prevalence of Langmuir circulation, Belcher et al. (2012) argued against this, reasoning that wind and waves are rarely in equilibrium and citing variability in the ratio of u_s to u_* as evidenced by the large range in their computed values of La across the world's oceans. Conversely, a number of observational studies have found u_s to scale linearly with u_* (Esters et al., 2018; Gargett and Grosch, 2014; Kitaigorodskii et al., 1983). In cases where u_s is linearly proportional to u_*, it follows that that La is relatively constant and thus L_L and L_M become linearly proportional as well, as $L_M = La^{-2} L_L$ (omitting the von Kármán constant).

A framework based on La and L_L is presented in Belcher et al. (2012) and has been used by both observational (Esters et al., 2017) and large eddy simulation (LES) studies (e.g. Li et al., 2019; Li and Fox-Kemper, 2017) to assess the relative contributions of wind-driven current shear, buoyancy forcing, and Langmuir circulation to the overall turbulence regime. This framework defines TKE as a linear combination of the three forcings, similarly to Equation 6,

$$\varepsilon\left(\frac{z}{h} = 0.5\right) = A_s \frac{u_*^3}{h} + A_L \frac{w_{*L}^3}{h} + A_c \frac{w_*^3}{h} \qquad 7.$$

where $w_{*_L} = (u_*^2 u_s)^{1/3}$ and $w_* = (B_0 h)^{\frac{1}{3}}$ are velocity scales for wave and buoyancy-forced turbulence and $A_s = 2\left(1 - e^{-\frac{1}{2}L_a}\right)$, $A_L = 0.22$, and $A_c = 0.3$ are coefficients derived from LES studies. This equation applies where z is half of h, an arbitrary depth chosen to discern where the three forcings are well established. A_s is made a function of L_a to account for the inhibition of vertical velocity shear and thus shear production by the enhanced vertical velocities associated with Langmuir circulation. Equation 7 is rearranged into a scaling relationship of the form

$$\frac{\varepsilon\left(\frac{z}{h}=0.5\right)}{\frac{u_*^3}{h}} = A_s + A_L La^{-2} \; + A_c La^{-2} \frac{h}{L_L} \; where \; B_0 > 0 \qquad 8.$$

which is used to define a turbulence regime diagram in $La - h/L_L$ space (e.g. Figure 2). The three "corners" of this diagram denote regimes where either wind, Langmuir, or buoyancy is the dominant forcing.

Here, we use both MO similarity and the more recent Belcher et al. (2012) framework to explore the scaling of ε estimates obtained from a moored Pulse-Coherent acoustic Doppler current velocity profiler (ADCP) in the Southeast Pacific Ocean Stratus region. Moored ADCP measurements represent a relatively new methodology (Zippel et al., 2021) that allows for the analysis of turbulence across an extended length of time and range of conditions. The moored nature of these measurements also allows for concurrent, in-situ measurements of wind, waves, and surface fluxes, which are not always possible in more standard deployments of ascending/descending profilers. The ADCP was deployed at 8.4 meters water depth on the Stratus Mooring at 20°S, 85°W in 2008-2010, as part of the Variability of American Monsoon Systems (VAMOS) Ocean–Cloud–Atmosphere–Land Study Regional Experiment (VOCALS-Rex) (Mechoso et al., 1995; Wood et al., 2011). The Stratus Mooring has been maintained by the Woods Hole Oceanographic Institution Upper Ocean Processes Group since 2000 and has been integral in efforts to characterize boundary layer processes in the Stratus region. Results from data collected at the mooring site are considered applicable over large swaths of the Stratus region, as it is known to lack synoptic forcing and exhibit relative uniformity in hydrographic surveys and wind fields (Holte et al., 2014; Weller et al., 2014).

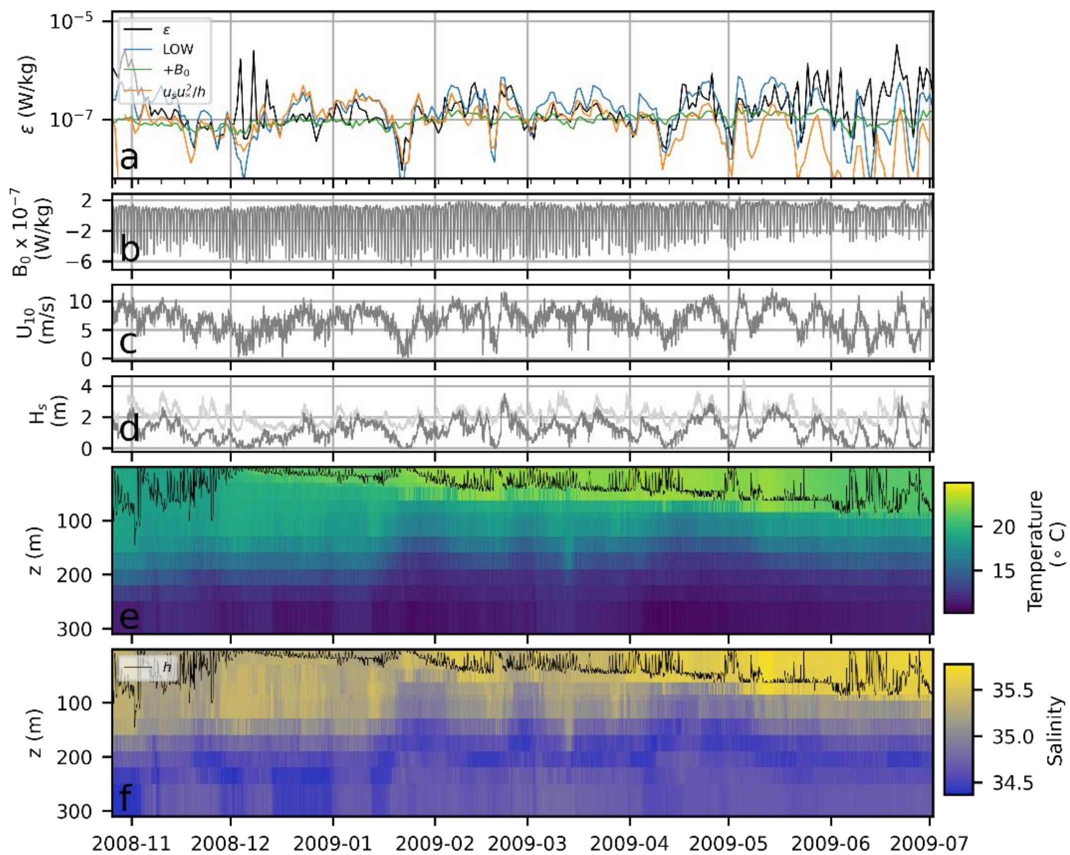

Figure 1. Time series of daily-averaged a) TKE dissipation rate (ε) overlaid with the Law of the Wall (LOW; Equation 2), destabilizing (positive) surface buoyancy flux ($+B_0$; Equation 3) and $u_s u_*^2/h$ scalings, b) surface buoyancy flux (B_0), c) wind speeds at 10 meters height (U_{10}), d) significant wave height (H_s) calculated from measured wave spectra (full

spectrum in light gray, wind-sea in dark gray), e) potential temperature and f) practical salinity, overlaid by mixed layer depth (*h*; black line)

2 Data and Methods

2.1 Pulse-coherent ADCP

Fine-scale velocity measurements were collected with a 2 MHz Nortek AquaDopp High-Resolution (HR) velocity profiler installed at 8.4 meters water depth on the mooring line and outfitted with a fin that allowed it to remain in-line with and facing the prevailing current (see Zippel et al., 2021). The AquaDopp HR is a pulse-to-pulse coherent ADCP that transmits two sequential pulses of which the phase shift allows for the calculation of radial velocities at centimeter-scale resolution. The specifics and validation of obtaining microstructure turbulence measurements using pulse-coherent ADCPs were first described in Veron and Melville (1999) and later in the context of moored deployments in Zippel et al. (2021). The instrument was fitted with a custom sensor head with 3 beams: two beams in a plane orthogonal to the cylindrical axis and a third beam directed upward 45° to this plane and 45° between the two horizontal orthogonal beams. The system was set to sample only Beam 1, orthogonal to the instrument axis and into the flow along the axis of the vane, in order to maximize the sample rate at 4 Hz. Profiles of along-beam velocities were 1.38 meters total in length and range-gated into 53 cells, each 26 millimeters in size. The nominal velocity range in each bin was ±10.5 cm s^{-1} and sampling occurred over 135 second "bursts" once every hour at a rate of 4 Hz for a total of 540 profiles per burst. Over 5000 bursts were collected in total over the study period.

2.2 Calculation of TKE dissipation rate

The AquaDopp HR appeared significantly bio-fouled upon recovery, so velocity measurements were truncated at 02-July-2009, shortly before the velocity and corresponding ping correlation values (a measure of strength-of-return) became erratic. The remaining data were quality-controlled and used to calculate ε following the methods detailed in Zippel et al. (2021). A simplified overview of these methods is provided here.

Data are first corrected for phase wrapping, an artifact associated with pulse-coherent ADCPs in which radial velocities exceeding a so-called ambiguity velocity "wrap around" and are recorded as abruptly high or low values in multiples of 2π. Then, "unwrapped" velocity profiles with an averaged ping correlation lower than 60% and individual pings with correlations lower than 40% are removed. Power spectra are calculated from the individual velocity profiles collected during each 135-second burst, then averaged together into a single, burst-averaged power spectrum. ε is estimated from the inertial subrange of each burst-averaged spectrum, defined as the region where the slope of the spectrum is equal to the theoretical -5/3 from Kolmogorov's "5/3" law for energy distribution in a turbulent fluid (Kolmogorov, 1941):

$$E(k) = C_1 \varepsilon^{2/3} k^{-5/3} \qquad 9.$$

Here, $E(k)$ is the power spectral density of turbulent velocities in the inertial subrange, k is wavenumber, and $C_1 = 0.53$ (Sreenivasan, 1995). Values of ε below $10^{-9}\ W/kg$ (constituting 3% of total data) are masked as they are likely close to the instrument noise floor, as reported for a similar pulse-coherent ADCP configuration in Zippel et al. (2021).

2.3 Temperature, salinity, and mixed layer depth

Temperature and salinity were measured from a suite of conductivity-temperature loggers installed on the mooring line at depths of 0.85, 3.7, 6.75, 16, 30, 37.5, 40, 62.5, 85, 96.3, 130, 160, 190, 220, 250, and 310 meters. Four different sensor models were used: RBR XR-420, Sea-Bird Electronics (SBE)-39, SBE-16, and SBE-37. Mixed layer depth, h, was calculated using hourly-averaged temperature measurements interpolated over half meter intervals, and defined to extend down to the depth at which temperature first differs by 0.1 degrees from the surface.

2.4 Meteorological measurements

Wind speed, wind direction, air temperature, humidity, shortwave radiation, and longwave radiation were recorded once per minute from an Improved Meteorological (IMET) sensor suite installed on the buoy about 2.7 meters above sea surface (Colbo and Weller, 2009). Buoyancy flux, defined as positive out of the ocean and in units of *W/kg*, was calculated as

$$B_0 = -\frac{g\alpha Q_{net}}{\rho c_p} + g\beta(E-P)S_0 \qquad 10.$$

where g is gravity, α is the thermal expansion coefficient, Q_{net} is surface heat flux, ρ is ocean density, c_p is the specific heat of water, β is the haline contraction coefficient, E and P are the rates of evaporation and precipitation, and S_0 is the surface salinity. P, measured using a rain gauge on the buoy, was effectively 0 ms^{-1} across the entire study period. Q_{net} is calculated as the net sum of the shortwave, net longwave, latent, and sensible fluxes. Net longwave radiation and the turbulent heat fluxes were calculated using version 3.6 of the COARE bulk flux algorithm (Fairall et al., 2003, 1996). Only the amount of shortwave radiation absorbed in the mixed layer (I) is used in the calculation of Q_{net}, which can at times exclude upwards of 20% of the total incoming radiation (I_0). This is calculated as:

$$I = I_0 - \left[I_0(I_1 e^{-\frac{h}{\lambda_1}} + I_2 e^{-\frac{h}{\lambda_2}}\right] \qquad 11.$$

where subscripts 1 and 2 indicate the shortwave and longwave components of insolation, following Price et al. (1986). $I_1 = 0.62, I_2 = 1 - 0.62, \lambda_1 = 0.6m,\ \lambda_2 = 20m$ for fairly clear, mid-ocean water (Paulson and Simpson, 1977). COARE was also used to calculate E and wind stress ($\tau = \rho\overline{u'w'}$). Water-side friction velocity was calculated as $u_* = \left(\frac{|\tau|}{\rho}\right)^{\frac{1}{2}}$ and α , c_p , β and ρ were calculated with the Gibbs Seawater Oceanographic Toolbox.

2.5 Wave measurements

Wave data were acquired from the National Buoy Data Center (NBDC) wave and marine data acquisition system (WAMDAS; Teng et al. (2005)) installed on the mooring's 2.7m-diameter surface buoy. The inertial measurement unit for the WAMDAS was installed inside the buoy, near the water line. Two-dimensional wave frequency spectra were calculated from the wave spectral density and Longuet-Higgins Fourier Coefficients provided for the Stratus mooring station by the NBDC. The measured frequencies ranged from 0.020 to 0.485 Hz and higher frequencies are estimated using an f^{-5} spectral tail calculated according to Appendix B of Webb and Fox-Kemper (2015). Though patching on an f^{-5} tail is a standard method of extending the spectra beyond what is feasibly measured, we recognize that it may result in an underestimation of Stokes drift on the order of ~10-30% if the highest measured ("cut-off") frequency is lower than that of the transition between equilibrium and saturation ranges (Lenain and Pizzo, 2020). Stokes drift at the surface is calculated as

$$u_s|_{z=0} \approx \frac{16\pi^3}{g}\int_0^\infty \int_{-\pi}^{\pi}(cos\theta, sin\theta, 0)f^3 S_{f\theta}(f,\theta)d\theta df \qquad 12.$$

where f is frequency and $S_{f\theta}$ is the directional wave spectrum. To obtain the component of the Stokes drift in the direction of the wind, Equation 12 is multiplied by the cosine of the difference between the direction of Stokes drift with that of the wind. From here onward, u_s denotes the component of the surface Stokes drift in the direction of the wind.

The wind-sea separation frequency was calculated systematically using methods described in Wang and Hwang (2001) and Hwang et al. (2011). Significant wave height of the wind-sea, H_{sw}, is defined as $\frac{1}{4}\sqrt{m_0}$, where m_0 is the zeroth integral moment of the 1-D wave spectral density of the wind-sea spectra. Phase speed is calculated as $c_p = 1.56/f_{peak}$, where f_{peak} is the peak frequency of the wind-sea. The wave transition depth is defined in Terray et al. (1996) as $z_t = 0.3\kappa\bar{c}/u_*$, where $\bar{c}$ is an effective phase speed related to the flux of energy from wind stress into the wave field. We use the approximation $\bar{c} = \frac{1}{2}c_p$, which represents an upper-bound estimate.

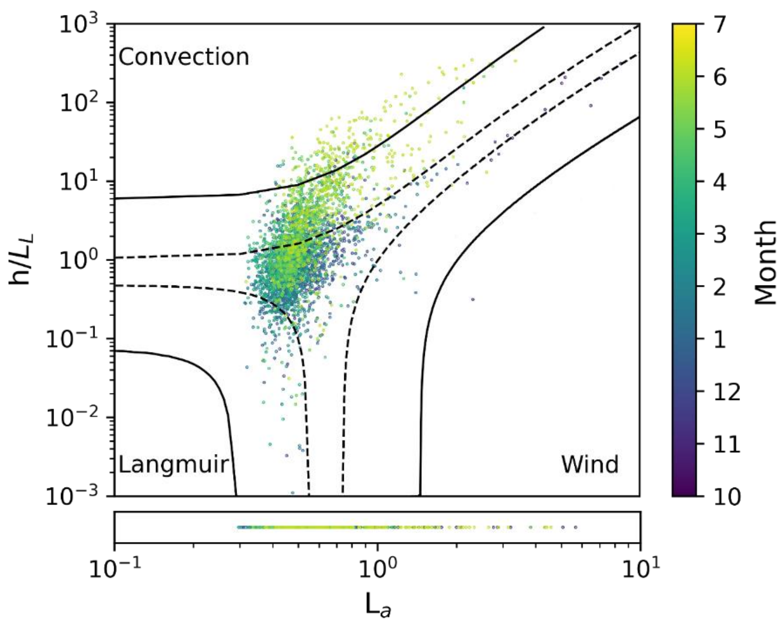

Figure 2. Turbulence regime diagram showing the relative contributions to TKE by convection, Langmuir circulation, and wind-generated current shear, after Belcher et al. (2012). Data are colored by the calendar month during which they were collected, with partial data from July and October and no data from August and September. Solid and dashed lines indicate regions where 90% and 60%, respectively, of overall TKE is generated by a single forcing, as calculated from Equation 8. The regime diagram is defined only for destabilizing B_0, so data in stabilizing conditions are shown in 1-dimensional L_a space below.

3 Results

3.1 Conditions at the Stratus Mooring Site

Monthly-averaged destabilizing buoyancy fluxes are strongest in May and June ($\sim 1.5 \times 10^{-7} Wkg^{-1}$), and weakest in the austral summer months ($\sim 8 \times 10^{-8} Wkg^{-1}$) (Figure 1b). The average hourly change in wind direction is 7.4°, in line with the remarkably directionally steady trade wind regime noted by Weller (2015). The magnitude of wind forcing is also fairly steady across the study period, with an average $U_{10} = 6.7ms^{-1}$, standard deviation of $2.2ms^{-1}$, and average hourly change of 0.64 ms^{-1} (Figure 1c). However, there are several days-long periods where wind speeds drop to near-zero across the study period, such as in late January and mid-May. Trade winds in the region are driven by a high pressure cell to the southwest of the mooring, and dip when this cell is shifted and its associated pressure gradient is weakened (Weller et al., 2014). Dissipation rate drops in response to these dips in wind speed, though the magnitude of this response is variable (Figure 1a).

Spectra show the wind-sea to propagate primarily to the northwest whereas swell, originating from storms in the South Pacific, is primarily to the northeast. The equilibrium state of wind and wind-sea can be inferred with wave age, $\frac{c_p}{U_{10}}$, with young seas where $\frac{c_p}{U_{10}} < 0.8$, mature seas where $0.8 < \frac{c_p}{U_{10}} < 2$, and old seas where $\frac{c_p}{U_{10}} > 2$ (Edson et al., 2007). The average wave age of the wind-sea for conditions of $U_{10} > 3ms^{-1}$ is 1.8 with a standard deviation of 1, suggesting the prevalence of mature seas at the mooring site. There is a clear linear dependence between u_s and u_*, with $u_s = 5.5u_* + 9 \times 10^{-3}$ and an r^2 value of 0.62 (Supplemental Figure 1). From November through May, La averages to 0.51 with a standard deviation of 0.16. In June, the average and standard deviation are higher, at 0.86 and 0.72, respectively. Temperature and salinity data show the presence of the cold, fresh (11-13° C, 34.1-34.3; Schneider et al., 2003) Eastern South Pacific Intermediate Water (ESPIW) underlying the mixed layer at about ~200 m. The mixed layer depth broadly tracks the seasonal increase in destabilizing buoyancy fluxes and is modulated on shorter time scales by wind speed; e.g. the abrupt shoaling of the mixed layer depth that coincides with a drop in wind speeds that occurs in late January (Figure 1e,f).

Daily-averaged ε is shown in Figure 1a, overlain with daily-averaged LOW, destabilizing B_0 , and $u_*^2 u_s/h$. There are periods of time, such as in late December, where B_0 clearly captures the magnitude of ε more closely than LOW or w_{*L}/h. Late February is an example of where the opposite is true. There are also periods where $u_*^2 u_s/h$ matches the magnitude of ε more closely than LOW (all of March), and vice versa (late May). This is indicative of differing turbulence regimes at the mooring site, which are illustrated by Figure 2. In this diagram, the relative contributions of destabilizing surface buoyancy flux, wind-driven current shear, and Langmuir processes to the turbulence regime are calculated according to Equation 8 and colored by month to highlight variability across seasons. Stabilizing buoyancy flux conditions are represented in 1-dimensional L_a space below. As in Belcher et al. (2012) and following (Leibovich, 1983), L_a is calculated only for values of U_{10} above 3 m/s, which excludes 3% of data in conditions of destabilizing B_0 and 8% in conditions of stabilizing B_0. The black lines indicate regions where a single forcing is the dominant mechanism of turbulence production; the dotted and solid lines ostensibly indicate a 60% and 90% contribution, respectively, to overall turbulence, as calculated from ratios of the terms in Equation 8. Turbulence appears more buoyancy-forced in the austral winter months (yellow) than during the rest of the study period, when a mix of buoyant- and Langmuir-forced conditions prevail.

Study	Setting	Instrumentation	Scaling relationship for ε
Wyngaard & Coté (1971)	ABL; Wheat field	Hot-wire anemometer	$\frac{\varepsilon\kappa z}{u_*^3} = [1 + 0.5\lvert\frac{z}{L}\rvert^{2/3}]^{3/2} \quad where\ \frac{z}{L_M} < 0$ $\frac{\varepsilon\kappa z}{u_*^3} = [1 + 2.5\lvert\frac{z}{L}\rvert^{3/5}]^{3/2} \quad where\ \frac{z}{L_M} > 0$
Edson & Fairall (1998)	Marine ABL; Northeast Pacific, Northwest Atlantic	Sonic anemometer	$\frac{\varepsilon\kappa z}{u_*^3} = \frac{1 - \frac{z}{L_M}}{1 - 7\frac{z}{L_M}} - \frac{z}{L_M} \quad where\ \frac{z}{L_M} < 0$ $\frac{\varepsilon\kappa z}{u_*^3} = 1 + 5\frac{z}{L_M} \quad where\ \frac{z}{L_M} > 0$
Lombardo & Gregg (1989)	Northeast Pacific	Descending microstructure profiler	$\varepsilon = 1.76\frac{u_*^3}{\kappa\lvert z\rvert} + 0.58B_0 \quad where\ \frac{h}{L_M} > 0$
Esters et al. (2018)	Subtropical and North Atlantic, Arctic Ocean	Ascending microstructure profiler	$\varepsilon = 0.63\left(0.90\frac{u_*^3}{\kappa\lvert z\rvert} + 0.91B_0\right) \quad where\ \frac{h_\varepsilon}{L_L} > 1$
Callaghan et al. (2014)	Indian Ocean	Ascending microstructure profiler	$\varepsilon = 0.73\frac{u_*^3}{\kappa\lvert z\rvert} + 0.81B_0 \quad where\ B_0 > 0$
Tedford et al. (2014)	Lake Pleasant, New York	Ascending temperature-gradient microstructure profiler	$\varepsilon = 0.56\frac{u_*^3}{\kappa\lvert z\rvert} + 0.77B_0 \quad where\ B_0 > 0$

Table 1. Scaling relationships examined in Figure 3.

3.2 Scaling of ε

Measurements of ε binned by z/h show a marked deviation from the LOW, buoyancy flux, and $u_*^2 u_s/h$ scalings when the instrument is very near to ($\frac{z}{h}$~1) and very far from ($\frac{z}{h} \ll 1$) the base of the mixed layer (Supplemental Figure 2). Because moored pulse-coherent ADCPs are at a fixed depth and may remain near the top or bottom of the mixed layer for significant periods of time, boundary processes may considerably influence measured dissipation. Such processes at the base of the mixed layer include internal wave breaking and inertial shear, and at its upper bound bordering the transition zone, surface wave breaking. While the depth of our instrument is consistently 3-4 times that of H_{sw} and therefore out of the direct influence of breaking wave turbulence, calculation of z_t from Terray et al. (1996) suggests that up to 10% of data may be influenced by wave breaking turbulence transported downwards from the breaking layer. As a heuristic means of minimizing the influence of turbulent processes other than current shear, buoyancy flux, and Langmuir circulation in our scaling analysis, we examine the scaling of ε by LOW, buoyancy flux, and $u_*^2 u_s/h$ in the range of $0.135 < \frac{z}{\mathrm{h}} < 0.5$, which includes ~60% of measurements in destabilizing conditions (turbulence is generated) and ~40% in stabilizing conditions (turbulence is suppressed). These cutoffs correspond to $\frac{z}{\mathrm{h}}$ bins below and above which the large deviations of ε from these scalings are evident (Supplemental Figure 2).

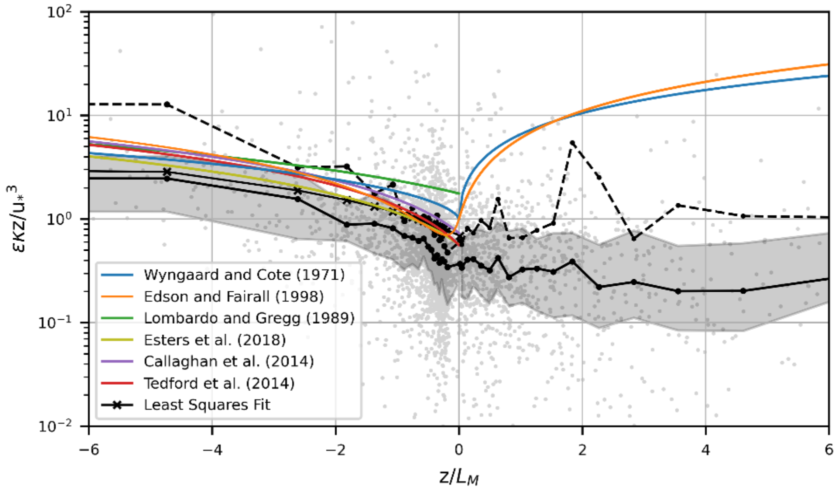

Figure 3. Measurements of ε (away from the boundaries of the mixed layer; $0.135 < \frac{z}{h} < 0.5$) scaled by Law of the Wall (Equation 2) across z/L_M regimes. Negative z/L_M corresponds to destabilizing conditions. The mean and median of bins containing equal numbers of data are denoted by the dashed and solid black lines, respectively. The shaded region indicates the interquartile range. The overlaid MO scaling relationships are defined in Table 1 and the least squares fit by Equation 13.

3.2.1 Shear and buoyancy regimes

Scaled ε is shown across z/L_M regimes in Figure 3, overlaid with bin-averaged mean and median. A least squares regression to Equation 6 of data excluding outlying values of $\frac{\varepsilon\kappa z}{u_*^3}$ (the highest and lowest 1%) returns:

$$\frac{\varepsilon\kappa z}{u_*^3} = 0.69 - 0.46 z/L_M \qquad 13.$$

Also overlaid are scaling relationships developed in prior studies of the ABL (Edson and Fairall, 1998; Wyngaard and Coté, 1971), OBL (Callaghan et al. 2014; Esters et al., 2018; Lombardo and Gregg, 1989) and lake surface boundary layer (Tedford et al., 2014). The scaling relationships, detailed in Table 1, are evaluated at each bin across the full z/L_M range of our data, though the actual ranges of data from which they were developed were either narrower or unspecified. We note that the scaling relationship from Esters et al. (2018) is defined for conditions of buoyancy dominance, $\frac{h_\varepsilon}{L_L} > 1$, where h_ε is the active mixing layer, though we present it across all data where $B_0 > 0$. In destabilizing conditions, these scaling relationships describe the binned mean and least squares fit of our data well where $|z/L_M| < 1$, but diverge at greater values, where they

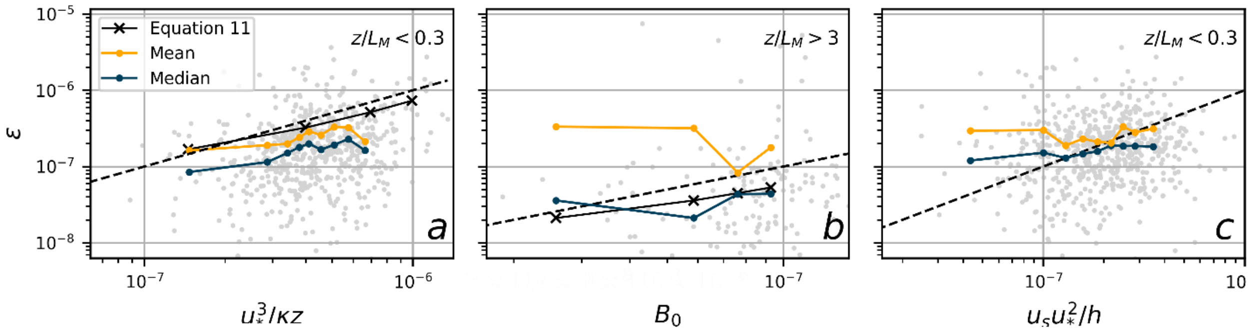

Figure 4. Measurements of ε (away from the boundaries of the mixed layer; $0.135 < \frac{z}{h} < 0.5$) in destabilizing conditions plotted directly against the Law of the Wall (Equation 2), surface buoyancy flux (Equation 3), and $u_s u_*^2/h$ scalings. Dominant forcing regimes are defined using z/L_M, with $\frac{z}{L_M} < 0.3$ denoting a buoyancy-dominant regime and $\frac{z}{L_M} > 3$ denoting a shear-dominant regime. The dashed black line corresponds to a 1:1 line. Bins contain equal numbers of data points.

overestimate our bin-averaged ε. In stabilizing conditions, there is little variability in the binned mean and median of scaled ε across z/L_M regimes and the data are poorly described by the MO similarity relationships.

Measurements of ε in destabilizing conditions are shown plotted directly against the LOW, surface buoyancy flux, and $\frac{u_s u_*^2}{h}$ scalings in regimes defined by z/L_M in Figure 4 and by h/L_L in Figure 5. Each scaling is compared only against data that falls in its respective dominance regime; for LOW and the Langmuir scaling, this is defined as $\frac{z}{L_M} < 0.3$ and $\frac{h}{L_L} < 0.5$ and for buoyancy-flux, $\frac{z}{L_M} > 3$ and $\frac{h}{L_L} > 5$. A 1:1 line is shown in each panel to represent idealized conditions where the scaling and measured ε are equivalent. In addition, Equation 13 is shown in Figures 4a-b calculated with bin-averaged LOW and B_0. MO similarity relationships are intended to capture the varying influence of shear and buoyancy-driven turbulence along the continuum of $\frac{z}{L_M}$ rather than in discrete regimes, therefore Equation 13 likely better represents

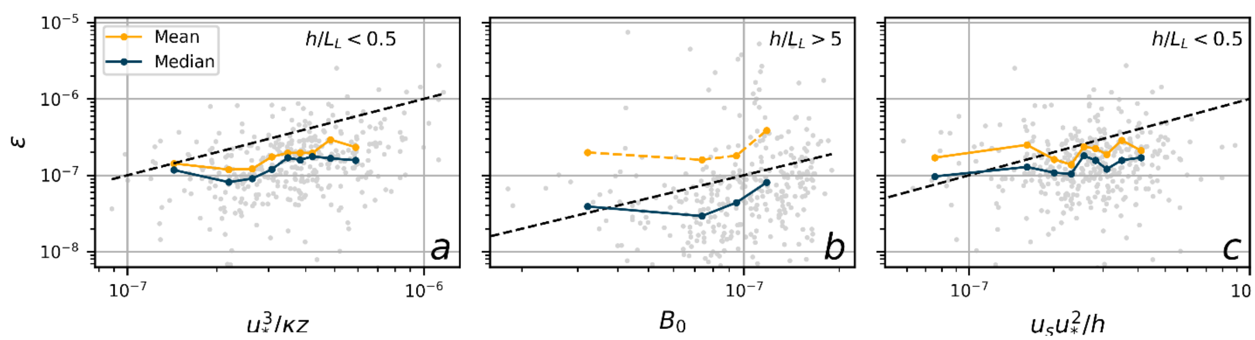

Figure 5 Same as Figure 4 but with regimes defined by $\frac{h}{L_L} < 0.5$ (buoyancy-dominant regime) and $\frac{h}{L_L} > 5$ (shear-dominant regime).

real conditions than a 1:1 line. Indeed, it better describes the slopes of the bin-averaged mean and median than the 1:1 line in Figure 4a, though the comparison is less clear in Figure 4b.

Destabilizing conditions	**All**	$\lvert\frac{h}{L_L}\rvert < 0.5$ **(Shear dominant)**	$\lvert\frac{z}{L_M}\rvert < 0.3$ **(Wind dominant)**	$\lvert\frac{h}{L_L}\rvert > 5$ **(B_0 dominant)**	$\lvert\frac{z}{L_M}\rvert > 3$ **(B_0 dominant)**
n	2226	400	517	368	149
$\boldsymbol{\varepsilon z\kappa/u_*^3}$					
Median	0.56	**0.40**	**0.38**	1.36	2.86
Mean	2.45	**0.67**	**0.60**	10.04	20.90
Q75 – Q25	1.13	**0.50**	**0.48**	2.77	6.55
$\boldsymbol{\varepsilon/B_0}$					
Median	1.05	1.52	1.60	**0.63**	**0.61**
Mean	2.79	3.31	3.87	**2.87**	**2.49**
Q75 – Q25	1.96	2.04	2.31	**1.16**	**0.86**
$\boldsymbol{\varepsilon h/u_s u_*^2}$					
Median	1.32	**0.56**	**0.83**	8.10	12.11
Mean	21.20	**1.03**	**6.48**	123.75	243.37
Q75 – Q25	3.27	**0.62**	**1.27**	20.91	42.50

Table 2. Median, mean, and interquartile range (Q75-Q25) of ε scaled by the Law of the Wall (Equation 2), surface buoyancy flux (Equation 3), and $u_s u_*^2/h$ scalings in destabilizing conditions ($B_0 > 0$). Only data away from the boundaries of the mixed layer ($0.135 < \frac{z}{h} < 0.5$) are considered.

To quantify the relationship between each scaling and measured ε, we present summary statistics of scaled ε in destabilizing conditions (Table 2) and stabilizing conditions (Table 3). Statistics are bolded for each scaling in their respective dominance regimes (as defined above). LOW consistently scales ε to an average of $\sim$0.65 across destabilizing and stabilizing conditions in “shear-dominant” regimes, which we use to describe the wind- and wind-wave-dominant regimes defined by z/L_M and h/L_L, respectively. B_0 scales ε to averages of 2.9 and 2.5 in destabilizing, buoyancy-dominant conditions defined by z/L_M and h/L_L, respectively. The $u_s u_*^2/h$ scaling is less consistent, scaling ε to averages of 1.03 and 6.5 in stabilizing, shear-dominant conditions. Notably, the interquartile range, which contains 50% of all data and describes their spread about the median, is reduced for each scaling in its dominant regime relative to the entire dataset, and increased in non-dominant regimes. For example, the interquartile range of ε scaled by LOW in Table 2 is decreased from ~1.1 to ~0.5 in the wind-dominant regimes but increased to upwards of 2 in the buoyancy-dominant regimes, where the scaling is not expected to apply. Effective scalings should collapse measurements of ε, so the observed decreases in the spread of data supports the use of these scaling as well as the ability of the Belcher and MO frameworks to delineate turbulence regimes.

Stabilizing conditions	**All**	$\lvert \frac{h}{L_L} < 0.5 \rvert$ **(Shear dominant)**	$\lvert \frac{z}{L_M} < 0.3 \rvert$ **(Wind dominant)**	$\lvert h/L_L > 5 \rvert$ **(B_0 dominant)**	$\lvert z/L_M > 3 \rvert$ **(B_0 dominant)**
n	1064	175	177	318	247
$\boldsymbol{\varepsilon z \kappa / u_*^3}$					
Median	0.34	**0.35**	**0.37**	0.38	0.35
Mean	3.41	**0.61**	**0.69**	9.55	11.78
Q75 – Q25	0.78	**0.49**	**0.51**	0.86	0.97
$\boldsymbol{\varepsilon h / u_s u_*^2}$					
Median	0.77	**0.64**	**0.84**	1.10	0.79
Mean	34.89	**1.55**	**2.37**	115.65	130.78
Q75 – Q25	1.72	**0.76**	**1.16**	4.86	3.48

Table 3. Same as in Table 2, but in stabilizing conditions ($B_0 < 0$).

3.2.2 Dependence on La

That the calculated statistics for LOW and B_0 vary relatively little in Tables 2 and 3 between z/L_M and h/L_L regimes suggests that the distinction between a wind-dominant regime, defined by z/L_M, and a Langmuir-dominant regime, defined by h/L_L, is unimportant in the Stratus region. This is tied to the low variability seen in La over most of the study period, which results in the linear dependency between L_L and L_M ($L_M \propto La^{-2} L_L$) shown in Figure 6. This relationship is described well by a least squares regression with a slope of 1.83 and an r^2 value of 0.88. Figure 7 shows ε scaled by Equation 13, calculated from binned values of LOW and B_0, in La space. Scaling by Equation 13 removes variability tied to B_0 and u_*, so if Langmuir effects were not sufficiently accounted for by LOW, we would expect to see a large deviation from unity at lower values of La, where Langmuir forcing is stronger. Instead, there is very little variability in La space, suggesting that La offers little to no additional predictive power over u_* at this field site.

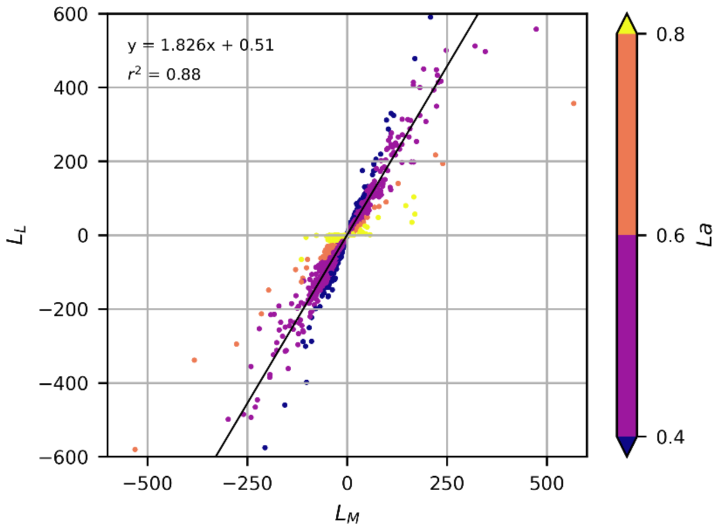

Figure 6. Least squares linear regression of L_L against L_M, illustrating the relationship $L_M \propto La^{-2} L_L$. Colors highlight the variation in slope associated with different values of binned La.

Furthermore, for ε scaled by LOW, we see little change in calculated statistics in the shear-dominant regime in both destabilizing and stabilizing conditions when data coinciding with lower La values are excluded (Table 4). The median of scaled ε increases slightly from 0.4 to 0.54 in destabilizing conditions and remains ~0.3 in stabilizing conditions, regardless of the degree of exclusion. In destabilizing conditions, the mean increases as more data are excluded, but only because the influence of several outlying data points on the mean is strengthened with increasingly fewer data points.

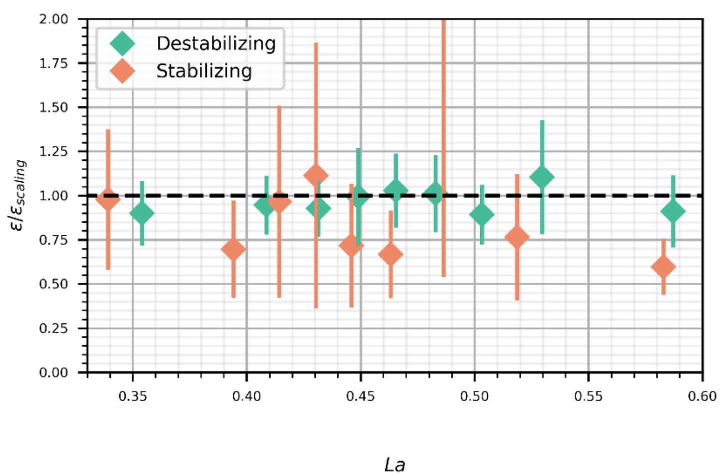

Figure 7. Bin-averaged measurements of ε (away from the boundaries of the mixed layer; $0.135 < \frac{z}{h} < 0.5$) scaled by Equation 13 in destabilizing conditions and Law of the Wall (Equation 2) in stabilizing conditions across La space. Because Equation 13 was fitted to data in which the highest and lowest 1% of values were excluded, the same filter is applied to the data in destabilizing conditions shown here. Each bin contains the same number of points. Vertical bars show the 95% confidence interval (1.96 multiplied by the standard error) of each bin.

$\boldsymbol{\varepsilon z \kappa / u_*^3}$

		Excluding $\boldsymbol{La} <\ 0.4$	**Excluding** $\boldsymbol{La} <\ 0.45$	**Excluding** $\boldsymbol{La} <\ 0.5$
$\boldsymbol{B_0 > 0}$, $\boldsymbol{\left\lvert \frac{h}{L_L} \right\rvert < 0.5}$				
n	400	*300*	*167*	*59*
Median	0.40	*0.42*	*0.44*	0.54
Mean	0.67	0.72	0.82	1.26
Q75 – Q25	0.50	0.51	0.52	0.60
$\boldsymbol{B_0 < 0}$, $\boldsymbol{\left\lvert \frac{h}{L_L} \right\rvert < 0.5}$				
n	175	*132*	*77*	*38*
Median	0.35	0.34	0.29	0.29
Mean	0.61	0.67	0.66	0.68
Q75 – Q25	0.49	0.49	0.54	0.72

Table 4. Median, mean, and interquartile range (Q75-Q25) calculated for ε scaled by LOW where subsets of data defined using the Langmuir number, La, are excluded in order to explore the distinction between Langmuir and current shear-forced regimes in our data. Only data that fall away from the boundaries of the mixed layer ($\boldsymbol{0.135 < \frac{z}{h} < 0.5}$) are considered.

4 Discussion

The Stratus region is characterized by directionally-steady southeast trade winds (Weller et al., 2014), which likely contributes to the observed linear relationship between u_s and u_* and an overall narrow range in La across the study period. The stronger the relationship between u_s and u_*, the more functionally equivalent w_{*L} and u_* become, a concept noted by Gargett and Grosch (2014). Therefore, at the Stratus mooring site, there appears to be little need to distinguish between wind-driven current shear- and Langmuir- dominant regimes in the context of turbulence scaling. We see a strong linear relationship between L_M and L_L and little difference in the normalization of ε by traditional MO scalings in regimes defined by $\frac{h}{L_L}$ compared to $\frac{z}{L_M}$. The mean, median, and interquartile range of $\varepsilon\kappa z/u_*^3$ are nearly identical across $\frac{h}{L_L}$ and $\frac{z}{L_M}$ wind-dominant regimes in both destabilizing and stabilizing conditions, as are the statistics for ε/B_0 for both buoyancy-dominant regimes in destabilizing conditions. The ability to consider current shear- and Langmuir-dominant regimes as a single “wind-wave”, or “shear-dominant”, regime, irrespective of La, may be relevant in efforts to improve the performance of coupled atmosphere-ocean general circulation models (GCMs) in the region, which suffer from systematic warm SST biases, in part due to poorly constrained upper-ocean processes (Lin, 2007; Ma et al., 1996;

Mechoso et al., 1995; Richter, 2015; Zheng et al., 2011; Zuidema et al., 2016). This may also be broadly applicable to turbulence scaling outside of the steadily-forced Stratus region: in a study of dissipation rates from microstructure profiler deployments at several sites ranging from the Arctic Ocean to the subtropical Atlantic ocean, Esters et al. (2018) found that the observed linear relationship between $u_*$and u_s allowed them to describe their data using a version of Equation 8 in which u_s is substituted by u_* multiplied by a constant factor.

While our analysis shows that ε scaling is not sensitive to the La regime, this does not mean that Langmuir circulation/turbulence is unimportant in the Stratus region, only that it is sufficiently accounted for by u_* (because of the linear relationship between u_* and u_s). Langmuir scaling has not been widely examined outside of modelling studies because of the difficulty in obtaining quality wave data concurrently with in-situ measurements of ε. That $u_s u_*^2/h$ appears to scale ε closer to unity than LOW for much of November-April (Figure 1a), which is perhaps surprising, as this scaling is a relatively new development (Grant and Belcher, 2009) and limited observational studies of the TKE budget have disagreed on the magnitude of the stokes production term relative to the dissipation term (Gerbi et al., 2009; Jarosz et al., 2021; Yoshikawa et al., 2018). Regardless, by June, the wind-sea weakens (monthly-averaged H_{sw} is 0.86m compared to ~1.2m across the whole study period) and the scaling grossly underestimates ε. Filtering out values of $H_{sw} < 1$, as well as $U_{10} < 5$ and $u_s < 0.03$, which would coincide with conditions of weak Langmuir forcing, does not systemically separate instances of significant underestimation of ε by $u_s u_*^2/h$ from instances where it performs well. Therefore, as discussed below, LOW serves as a more reliable scaling for ε in shear-dominant conditions, as its overestimation bias is fairly consistent and more easily corrected for.

In general, MO similarity works well in describing turbulence at the Stratus mooring site: LOW collapses the scatter of ε and scales it to an average of ~0.65 in shear-dominant conditions across both destabilizing and stabilizing conditions. The scaling of ε close to, but not exactly, unity is not uncommon in observational studies. For example, Callaghan et al. (2014) suggested that an observed overestimation of ε by LOW was due to a period of continually changing wind direction in which a misalignment of the wind and wave field reduced the effective wind stress on the ocean. Tedford et al., (2014) attributed overestimation by LOW in a lake setting to enhanced stratification brought on by the lateral advection of cool water. In our own data, we also see individual instances where LOW departs significantly from measurements of ε. For example, in mid-February and throughout June, LOW tracks a sudden dip in wind speed characteristic to the Stratus region, while measured ε remains at relatively elevated levels (Figure 1). These dips in wind speed have been observed to generate near-inertial oscillations (Weller et al., 2014) that can alter currents and impact the turbulence regime through the generation of additional current shear. Additionally, the persistence of the wind-sea and associated Langmuir circulation following a drop in winds can create a lag between wind stress and ε. However, there are also instances where measured ε plummets following a drop to near-zero winds (e.g. mid-January, mid April, early May), a change that is tracked remarkably well by LOW. While these sudden, short-term drops in wind speed do add some short-term complexity to the scaling of ε, the slight overestimation represented by the average $\frac{\varepsilon\kappa z}{u_*^3} = 0.65$ across the study period appears more systematic than the individual instances of dips in wind speed, and we hypothesize some possible causes: LES studies have shown the enhancement of vertical mixing associated with Langmuir circulation reduces vertical shear in the upper ocean, thus inhibiting current shear production of TKE (Belcher et al., 2012; Fan et al., 2020) and therefore reducing ε relative to the wind stress. Another possibility relates to the assumption of a constant stress layer upon which MO similarity theory and LOW rely. Observations (Gerbi et al., 2008) and linear surface stress scaling (e.g. Fisher et al., 2017) show stress to decay with depth according to $\tau_z = \tau(1-\frac{z}{h})$, suggesting LOW calculated from τ at the surface would overestimate shear turbulence at depth. When calculating LOW using decayed stress, τ_z, our measurements of ε (within the same $0.135 < \frac{z}{h} < 0.5$ range as before) are scaled with averages of 1.28 and 1.01 where $|\frac{h}{L_L}| < 0.5$ and 0.95 and 1.04 where $|\frac{z}{L_M}| < 0.3$, in destabilizing and stabilizing conditions, respectively. These values are notably closer to unity than ~0.65. There is little reason to assume the constant stress layer assumption holds at the 8.4 m depth of our measurements, and these calculations suggest that stress decay may be a factor in the deviation of the scaling of ε by LOW from unity in real-world conditions. Nevertheless, our results support the merit of classic MO scaling despite a possible violation of the constant stress layer assumption. Future work is needed to more fully assess if full flux-profile relationships are tenable outside of the constant stress layer, but within the ocean surface mixed layer.

As for the buoyancy flux scaling, scatter is collapsed in destabilizing, buoyancy-dominant conditions, but ε is overestimated by an average of ~2.5. The median of ~0.6 is closer to unity and the findings of other studies, such as ~0.58 in Lombardo and Gregg (1989) and 0.81 in (Anis and Moum, 1992), and indicates that most of the data are scaled near unity but that the mean is influenced by extreme outliers. This is likely the case because the Stratus mooring site does not experience true buoyancy-dominant conditions, which are typically defined as $|z/L_M| > 10$ (e.g. Lombardo and Gregg, 1989). Out of necessity, we defined a less conservative threshold of $|z/L_M| > 3$, which likely resulted in the influence of turbulent processes not captured by B_0.

Scaling relationships from prior studies describe the binned mean of our data well for destabilizing conditions of $\left|\frac{z}{L_M}\right| < 1$ (wind-dominant), except for those of Lombardo and Gregg (1989) and Wyngaard and Cote (1971). Lombardo and Gregg (1989) may differ from the other aquatic studies because it utilized a descending microstructure profiler that necessarily excluded data 5-10 meters near the surface, possibly excluding wave-related turbulence otherwise captured in our data and studies utilizing ascending profilers. Likewise, Edson and Fairall (1998), conducted in the ABL above the ocean, may have been influenced by wave activity while Wyngaard and Cote (1971) did not. Regardless, all of the relationships deviate from the binned mean of our data in destabilizing conditions of $|\frac{z}{L_M}| > 2$. This could be because in general, fewer data exist at greater values of $|\frac{z}{L_M}|$, making statistics and linear regressions derived from these data less universal. Furthermore, similarity relationship with coefficients derived from the scaling of ε by LOW and B_0 ostensibly describe wind-generated current shear and convective turbulence, but inadvertently capture the effects of many other processes that are potentially unique to the place and time of data collection, with the intermittent nature of turbulence adding additional complexity. Data collected in studies using microstructure profilers represent snapshots in time and are therefore perhaps more susceptible to this temporal and spatial variability, resulting in the large spread of functions derived from field estimates of ε.

5 Conclusion

Moored, pulse-coherent ADCP measurements of ε are a useful development in the study of ocean turbulence, allowing for analysis of turbulence across an extended range of conditions and length of time at a single site. Here, we use similarity scaling to explore 9 months of moored measurements of ε across a range of forcing conditions in the upper mixed layer of the Stratus mooring site. We find that:

- LOW scales ε well in shear-dominant conditions across both destabilizing and stabilizing conditions, as determined by a) its ability to collapse measurements of ε and b) the proximity of the mean or median of scaled ε to unity
- B_0 scales ε well in buoyancy-dominant conditions in destabilizing conditions, by the same standards as above
- $u_s u_*^2/h$ scales ε well for a large portion of the study period, but does very poorly in May and June. It is difficult to parse out the conditions in which it performs well, therefore LOW remains the more useful scaling in shear-dominant conditions
- h/L_L and z/L_M are functionally equivalent means for separating the shear-dominant regime from the buoyancy-dominant regime in the Stratus region because of the strong linear relationship between u_* and u_s
- Prior scaling relationships largely agree with our measurements in destabilizing conditions of $|z/L_M|$<1, but their deviation elsewhere highlights how field estimates of ε are susceptible to variability across space and time

Acknowledgments

Funding for early iterations of this project associated with VOCALS and the Stratus 9 mooring was provided by NSF (Awards 0745508, 0745442) and ONR (Grant N000141812431). The Stratus Ocean Reference Station is funded by the Global Ocean Monitoring and Observing Program of the National Oceanic and Atmospheric Administration (CPO FundRef Number 100007298), through the Cooperative Institute for the North Atlantic Region (CINAR) under Cooperative Agreement NA14OAR4320158. CJZ was supported by NSF through Grant Award Nos. 1756839 and 2049546. JTF and SZ were supported by NASA grants 80NSSC18K1494. SZ was additionally supported by NASA grant 80NSSC21K0832 and NSF Award No. 2023020. The authors declare no financial conflicts of interest in this work.

Open Research

Velocity, correlation, amplitude, and other outputs from the 2 MHz Nortek AquaDopp High-Resolution (HR) Pulse-Coherent ADCP are available at https://doi.org/10.7916/xs7h-b561. Data from the Stratus Ocean Reference Station are made freely available by the OceanSITES project (Send et al., 2010) and the national programs that contribute to it, and are obtained from https://dods.ndbc.noaa.gov/oceansites/). Wave data are hosted by the National Buoy Data Center and are obtained at https://www.ndbc.noaa.gov/station_page.php?station=32012. The MATLAB code used to quality control the ADCP data and calculate ε is available on GitHub at: https://github.com/zippelsf/MooredTurbulenceMeasurements. The Python code used to process meteorological and wave data and to generate figures is available from the author upon request.

Bibliography:

Agrawal, Y.C., Terray, E.A., Donelan, M.A., Hwang, P.A., Iii, A.J.W., Drennan, W.M., Kahma, K.K., Krtaigorodskii, S.A., 1992. Enhanced dissipation of kinetic energy beneath surface waves. Nature 359, 359219a0. https://doi.org/10.1038/359219a0

Anis, A., Moum, J.N., 1995. Surface Wave–Turbulence Interactions. Scaling $\epsilon(z)$ near the Sea Surface. J. Phys. Oceanogr. 25, 2025–2045. https://doi.org/10.1175/1520-0485(1995)025<2025:SWISNT>2.0.CO;2

Anis, A., Moum, J.N., 1992. The Superadiabatic Surface Layer of the Ocean during Convection. J. Phys. Oceanogr. 22, 1221–1227. https://doi.org/10.1175/1520-0485(1992)022<1221:TSSLOT>2.0.CO;2

Belcher, S.E., Grant, A.L.M., Hanley, K.E., Fox-Kemper, B., Roekel, L.V., Sullivan, P.P., Large, W.G., Brown, A., Hines, A., Calvert, D., Rutgersson, A., Pettersson, H., Bidlot, J.-R., Janssen, P.A.E.M., Polton, J.A., 2012a. A global perspective on Langmuir turbulence in the ocean surface boundary layer. Geophys. Res. Lett. 39. https://doi.org/10.1029/2012GL052932

Belcher, S.E., Grant, A.L.M., Hanley, K.E., Fox-Kemper, B., Van Roekel, L., Sullivan, P.P., Large, W.G., Brown, A., Hines, A., Calvert, D., Rutgersson, A., Pettersson, H., Bidlot, J.-R., Janssen, P.A.E.M., Polton, J.A., 2012b. A global perspective on Langmuir turbulence in the ocean surface boundary layer. Geophys. Res. Lett. 39, L18605. https://doi.org/10.1029/2012GL052932

Brainerd, K.E., Gregg, M.C., 1993. Diurnal restratification and turbulence in the oceanic surface mixed layer: 1. Observations. J. Geophys. Res. Oceans 98, 22645–22656. https://doi.org/10.1029/93JC02297

Callaghan, A.H., Ward, B., Vialard, J., 2014. Influence of surface forcing on near-surface and mixing layer turbulence in the tropical Indian Ocean. Deep Sea Res. Part Oceanogr. Res. Pap. 94, 107–123. https://doi.org/10.1016/j.dsr.2014.08.009

Colbo, K., Weller, R.A., 2009. Accuracy of the IMET Sensor Package in the Subtropics. J. Atmospheric Ocean. Technol. 26, 1867–1890. https://doi.org/10.1175/2009JTECHO667.1

Craig, P.D., Banner, M.L., 1994. Modeling Wave-Enhanced Turbulence in the Ocean Surface Layer. J. Phys. Oceanogr. 24, 2546–2559. https://doi.org/10.1175/1520-0485(1994)024<2546:MWETIT>2.0.CO;2

Craik, A.D.D., Leibovich, S., 1976. A rational model for Langmuir circulations. J. Fluid Mech. 73, 401–426. https://doi.org/10.1017/S0022112076001420

D'Asaro, E.A., 2014. Turbulence in the Upper-Ocean Mixed Layer [WWW Document]. Httpdxdoiorg101146annurev-Mar.-010213-135138. URL http://www.annualreviews.org/doi/10.1146/annurev-marine-010213-135138 (accessed 5.18.17).

Drennan, W.M., Kahma, K.K., Terray, E.A., Donelan, M.A., Kitaigorodskii, S.A., 1992. Observations of the Enhancement of Kinetic Energy Dissipation Beneath Breaking Wind Waves, in: Breaking Waves, International Union of Theoretical and Applied Mechanics. Springer, Berlin, Heidelberg, pp. 95–101. https://doi.org/10.1007/978-3-642-84847-6_6

Edson, J., Crawford, T., Crescenti, J., Farrar, T., Frew, N., Gerbi, G., Helmis, C., Hristov, T., Khelif, D., Jessup, A., Jonsson, H., Li, M., Mahrt, L., McGillis, W., Plueddemann, A., Shen, L., Skyllingstad, E., Stanton, T., Sullivan, P., Sun, J., Trowbridge, J., Vickers, D., Wang, S., Wang, Q., Weller, R., Wilkin, J., Williams, A.J., Yue, D.K.P., Zappa, C., 2007. The Coupled Boundary Layers and Air–Sea Transfer Experiment in Low Winds. Bull. Am. Meteorol. Soc. 88, 341–356. https://doi.org/10.1175/BAMS-88-3-341

Edson, J.B., Fairall, C.W., 1998. Similarity Relationships in the Marine Atmospheric Surface Layer for Terms in the TKE and Scalar Variance Budgets. J. Atmospheric Sci. 55, 2311–2328. https://doi.org/10.1175/1520-0469(1998)055<2311:SRITMA>2.0.CO;2

Esters, L., Breivik, Ø., Landwehr, S., Doeschate, A. ten, Sutherland, G., Christensen, K.H., Bidlot, J.-R., Ward, B., 2018. Turbulence Scaling Comparisons in the Ocean Surface Boundary Layer. J. Geophys. Res. Oceans 123, 2172–2191. https://doi.org/10.1002/2017JC013525

Esters, L., Landwehr, S., Sutherland, G., Bell, T.G., Christensen, K.H., Saltzman, E.S., Miller, S.D., Ward, B., 2017. Parameterizing air-sea gas transfer velocity with dissipation. J. Geophys. Res. Oceans 122, 3041–3056. https://doi.org/10.1002/2016JC012088

Fairall, C.W., Bradley, E.F., Hare, J.E., Grachev, A.A., Edson, J.B., 2003. Bulk Parameterization of Air–Sea Fluxes: Updates and Verification for the COARE Algorithm. J. Clim. 16, 571–591. https://doi.org/10.1175/1520-0442(2003)016<0571:BPOASF>2.0.CO;2

Fairall, C.W., Bradley, E.F., Rogers, D.P., Edson, J.B., Young, G.S., 1996. Bulk parameterization of air-sea fluxes for Tropical Ocean-Global Atmosphere Coupled-Ocean Atmosphere Response Experiment. J. Geophys. Res. Oceans, a 101, 3747–3764. https://doi.org/10.1029/95JC03205

Fan, Y., Yu, Z., Savelyev, I., Sullivan, P.P., Liang, J.-H., Haack, T., Terrill, E., de Paolo, T., Shearman, K., 2020. The effect of Langmuir turbulence under complex real oceanic and meteorological forcing. Ocean Model. 149, 101601. https://doi.org/10.1016/j.ocemod.2020.101601

Fisher, A.W., Sanford, L.P., Scully, M.E., Suttles, S.E., 2017. Surface Wave Effects on the Translation of Wind Stress across the Air–Sea Interface in a Fetch-Limited, Coastal Embayment. J. Phys. Oceanogr. 47, 1921–1939. https://doi.org/10.1175/JPO-D-16-0146.1

Gargett, A.E., Grosch, C.E., 2014. Turbulence Process Domination under the Combined Forcings of Wind Stress, the Langmuir Vortex Force, and Surface Cooling. J. Phys. Oceanogr. 44, 44–67. https://doi.org/10.1175/JPO-D-13-021.1

Gemmrich, J.R., Farmer, D.M., 2004. Near-Surface Turbulence in the Presence of Breaking Waves. J. Phys. Oceanogr. 34, 1067–1086. https://doi.org/10.1175/1520-0485(2004)034<1067:NTITPO>2.0.CO;2

Gerbi, G.P., Trowbridge, J.H., Edson, J.B., Plueddemann, A.J., Terray, E.A., Fredericks, J.J., 2008. Measurements of Momentum and Heat Transfer across the Air–Sea Interface. J. Phys. Oceanogr. 38, 1054–1072. https://doi.org/10.1175/2007JPO3739.1

Gerbi, G.P., Trowbridge, J.H., Terray, E.A., Plueddemann, A.J., Kukulka, T., 2009. Observations of Turbulence in the Ocean Surface Boundary Layer: Energetics and Transport. J. Phys. Oceanogr. 39, 1077–1096. https://doi.org/10.1175/2008JPO4044.1

Grant, A.L.M., Belcher, S.E., 2009. Characteristics of Langmuir Turbulence in the Ocean Mixed Layer. J. Phys. Oceanogr. 39, 1871–1887. https://doi.org/10.1175/2009JPO4119.1

Holte, J., Straneo, F., Farrar, J.T., Weller, R.A., 2014. Heat and salinity budgets at the Stratus mooring in the southeast Pacific. J. Geophys. Res. Oceans 119, 8162–8176. https://doi.org/10.1002/2014JC010256

Hwang, P.A., Ocampo-Torres, F.J., García-Nava, H., 2011. Wind Sea and Swell Separation of 1D Wave Spectrum by a Spectrum Integration Method. J. Atmospheric Ocean. Technol. 29, 116–128. https://doi.org/10.1175/JTECH-D-11-00075.1

Jarosz, E., Wijesekera, H.W., Wang, D.W., 2021. Coherent Velocity Structures in the Mixed Layer: Characteristics, Energetics, and Turbulent Kinetic Energy Budget. J. Phys. Oceanogr. 51, 2991–3014. https://doi.org/10.1175/JPO-D-20-0248.1

Kitaigorodskii, S.A., Donelan, M.A., Lumley, J.L., Terray, E.A., 1983. Wave-Turbulence Interactions in the Upper Ocean. Part II. Statistical Characteristics of Wave and Turbulent Components of the Random Velocity Field in the Marine Surface Layer. J. Phys. Oceanogr. 13, 1988–1999. https://doi.org/10.1175/1520-0485(1983)013<1988:WTIITU>2.0.CO;2

Kolmogorov, A., 1941. The Local Structure of Turbulence in Incompressible Viscous Fluid for Very Large Reynolds' Numbers. Akad. Nauk SSSR Dokl. 30, 301–305.

Leibovich, S., 1983. The form and Dynamics of Langmuir Circulations. Annu. Rev. Fluid Mech. 15, 391–427. https://doi.org/10.1146/annurev.fl.15.010183.002135

Lenain, L., Pizzo, N., 2020. The Contribution of High-Frequency Wind-Generated Surface Waves to the Stokes Drift. J. Phys. Oceanogr. 50, 3455–3465. https://doi.org/10.1175/JPO-D-20-0116.1

Li, Q., Fox-Kemper, B., 2017. Assessing the Effects of Langmuir Turbulence on the Entrainment Buoyancy Flux in the Ocean Surface Boundary Layer. J. Phys. Oceanogr. 47, 2863–2886. https://doi.org/10.1175/JPO-D-17-0085.1

Li, Q., Reichl, B.G., Fox-Kemper, B., Adcroft, A.J., Belcher, S.E., Danabasoglu, G., Grant, A.L.M., Griffies, S.M., Hallberg, R., Hara, T., Harcourt, R.R., Kukulka, T., Large, W.G., McWilliams, J.C., Pearson, B., Sullivan, P.P., Roekel, L.V., Wang, P., Zheng, Z., 2019. Comparing Ocean Surface Boundary Vertical Mixing Schemes Including Langmuir Turbulence. J. Adv. Model. Earth Syst. 11, 3545–3592. https://doi.org/10.1029/2019MS001810

Lin, J.-L., 2007. The Double-ITCZ Problem in IPCC AR4 Coupled GCMs: Ocean–Atmosphere Feedback Analysis. J. Clim. 20, 4497–4525. https://doi.org/10.1175/JCLI4272.1

Lombardo, C.P., Gregg, M.C., 1989a. Similarity scaling of viscous and thermal dissipation in a convecting surface boundary layer. J. Geophys. Res. Oceans 94, 6273–6284. https://doi.org/10.1029/JC094iC05p06273

Lombardo, C.P., Gregg, M.C., 1989b. Similarity scaling of viscous and thermal dissipation in a convecting surface boundary layer. J. Geophys. Res. Oceans 94, 6273–6284. https://doi.org/10.1029/JC094iC05p06273

Ma, C.-C., Mechoso, C.R., Robertson, A.W., Arakawa, A., 1996. Peruvian Stratus Clouds and the Tropical Pacific Circulation: A Coupled Ocean-Atmosphere GCM Study. J. Clim. 9, 1635–1645. https://doi.org/10.1175/1520-0442(1996)009<1635:PSCATT>2.0.CO;2

McWilliams, J.C., Sullivan, P.P., Moeng, C.-H., 1997. Langmuir turbulence in the ocean. J. Fluid Mech. 334, 1–30. https://doi.org/10.1017/S0022112096004375

Mechoso, C.R., Robertson, A.W., Neelin, J.D., 1995. The seasonal cycle over the tropical Pacific in coupled ocean-atmosphere General Circulation Models. Mon. Weather Rev. 123. https://doi.org/10.1175/1520-0493(1995)123<2825:TSCOTT>2.0.CO;2

Monin, A.S., Obukhov, A.M., 1959. Basic laws of turbulent mixing in the surface layer of the atmosphere.

Paulson, C.A., Simpson, J.J., 1977. Irradiance Measurements in the Upper Ocean. J. Phys. Oceanogr. 7, 952–956. https://doi.org/10.1175/1520-0485(1977)007<0952:IMITUO>2.0.CO;2

Price, J.F., Weller, R.A., Pinkel, R., 1986. Diurnal cycling: Observations and models of the upper ocean response to diurnal heating, cooling, and wind mixing. J. Geophys. Res. Oceans 91, 8411–8427. https://doi.org/10.1029/JC091iC07p08411

Richter, I., 2015. Climate model biases in the eastern tropical oceans: causes, impacts and ways forward. WIREs Clim. Change 6, 345–358. https://doi.org/10.1002/wcc.338

Schneider, W., Fuenzalida, R., Rodríguez-Rubio, E., Garcés-Vargas, J., Bravo, L., 2003. Characteristics and formation of Eastern South Pacific Intermediate Water. Geophys. Res. Lett. 30. https://doi.org/10.1029/2003GL017086

Send, U., Weller, R.A., Wallace, D.W.R., Chavez, F., Lampitt, R.L., Dickey, T., Honda, M., Nittis, K., Lukas, R., McPhaden, M.J., Feely, R.A., 2010. OceanSITES, in: Proceedings of OceanObs'09: Sustained Ocean Observations and Information for Society (Vol 2). Hall, J., Harrison, D.E. & Stammer, D., Eds., ESA Publication WPP-306, Venice, Italy, 21-25 September 2009. https://doi.org/10.5270/OceanObs09.cwp.79

Shay, T.J., Gregg, M.C., 1986. Convectively Driven Turbulent Mixing in the Upper Ocean. J. Phys. Oceanogr. 16, 1777–1798. https://doi.org/10.1175/1520-0485(1986)016<1777:CDTMIT>2.0.CO;2

Soloviev, A., Lukas, R., 2003. Observation of wave-enhanced turbulence in the near-surface layer of the ocean during TOGA COARE. Deep Sea Res. Part Oceanogr. Res. Pap. 50, 371–395. https://doi.org/10.1016/S0967-0637(03)00004-9

Sreenivasan, K.R., 1995. On the universality of the Kolmogorov constant. Phys. Fluids 7, 2778–2784. https://doi.org/10.1063/1.868656

Stips, A., Burchard, H., Bolding, K., Prandke, H., Simon, A., Wüest, A., 2005. Measurement and simulation of viscous dissipation in the wave affected surface layer. Deep Sea Res. Part II Top. Stud. Oceanogr., Observations and modelling of mixed layer turbulence: Do they represent the same statistical quantities? 52, 1133–1155. https://doi.org/10.1016/j.dsr2.2005.01.012

Stull, R.B., 1988. An introduction to boundary layer meteorology, Atmospheric sciences library. Kluwer Academic Publishers, Dordrecht ; Boston.

Sutherland, G., Christensen, K.H., Ward, B., 2014. Evaluating Langmuir turbulence parameterizations in the ocean surface boundary layer. J. Geophys. Res. Oceans 119, 1899–1910. https://doi.org/10.1002/2013JC009537

Sutherland, P., Melville, W.K., 2015. Field Measurements of Surface and Near-Surface Turbulence in the Presence of Breaking Waves. J. Phys. Oceanogr. Boston 45, 943–965.

Tedford, E.W., MacIntyre, S., Miller, S.D., Czikowsky, M.J., 2014. Similarity scaling of turbulence in a temperate lake during fall cooling. J. Geophys. Res. Oceans 119, 4689–4713. https://doi.org/10.1002/2014JC010135

Teng, C.-C., Bernard, L., Taft, B., Burdette, M., 2005. A compact wave and ocean data buoy system, in: Proceedings of OCEANS 2005 MTS/IEEE. Presented at the Proceedings of OCEANS 2005 MTS/IEEE, pp. 1249-1254 Vol. 2. https://doi.org/10.1109/OCEANS.2005.1639926

Terray, E. a., Donelan, M. a., Agrawal, Y. c., Drennan, W. m., Kahma, K. k., Williams, A. j., Hwang, P. a., Kitaigorodskii, S. a., 1996. Estimates of Kinetic Energy Dissipation under Breaking Waves. J. Phys. Oceanogr. 26, 792–807. https://doi.org/10.1175/1520-0485(1996)026<0792:EOKEDU>2.0.CO;2

Thorpe, S.A., 2005. The Turbulent Ocean. Cambridge University Press.

Van Roekel, L.P., Fox-Kemper, B., Sullivan, P.P., Hamlington, P.E., Haney, S.R., 2012. The form and orientation of Langmuir cells for misaligned winds and waves. J. Geophys. Res. Oceans 117. https://doi.org/10.1029/2011JC007516

Veron, F., Melville, W.K., 1999. Pulse-to-Pulse Coherent Doppler Measurements of Waves and Turbulence. J. Atmospheric Ocean. Technol. 16, 1580–1597. https://doi.org/10.1175/1520-0426(1999)016<1580:PTPCDM>2.0.CO;2

Wang, D.W., Hwang, P.A., 2001. An Operational Method for Separating Wind Sea and Swell from Ocean Wave Spectra. J. Atmospheric Ocean. Technol. 18, 2052–2062. https://doi.org/10.1175/1520-0426(2001)018<2052:AOMFSW>2.0.CO;2

Webb, A., Fox-Kemper, B., 2015. Impacts of wave spreading and multidirectional waves on estimating Stokes drift. Ocean Model., Waves and coastal, regional and global processes 96, 49–64. https://doi.org/10.1016/j.ocemod.2014.12.007

Weller, R.A., 2015. Variability and Trends in Surface Meteorology and Air–Sea Fluxes at a Site off Northern Chile. J. Clim. 28, 3004–3023. https://doi.org/10.1175/JCLI-D-14-00591.1

Weller, R.A., Majumder, S., Tandon, A., 2014. Diurnal Restratification Events in the Southeast Pacific Trade Wind Regime. J. Phys. Oceanogr. 44, 2569–2587. https://doi.org/10.1175/JPO-D-14-0026.1

Wood, R., Mechoso, C.R., Bretherton, C.S., Weller, R.A., Huebert, B., Straneo, F., Albrecht, B.A., Coe, H., Allen, G., Vaughan, G., Daum, P., Fairall, C., Chand, D., Gallardo Klenner, L., Garreaud, R., Grados, C., Covert, D.S., Bates, T.S., Krejci, R., Russell, L.M., Szoeke, S. de, Brewer, A., Yuter, S.E., Springston, S.R., Chaigneau, A., Toniazzo, T., Minnis, P., Palikonda, R., Abel, S.J., Brown, W.O.J., Williams, S., Fochesatto, J., Brioude, J., Bower, K.N., 2011. The VAMOS Ocean-Cloud-Atmosphere-Land Study Regional Experiment (VOCALS-REx): goals, platforms, and field operations. Atmospheric Chem. Phys. 11, 627–654. https://doi.org/10.5194/acp-11-627-2011

Wyngaard, J.C., Coté, O.R., 1971. The Budgets of Turbulent Kinetic Energy and Temperature Variance in the Atmospheric Surface Layer. J. Atmospheric Sci. 28, 190–201. https://doi.org/10.1175/1520-0469(1971)028<0190:TBOTKE>2.0.CO;2

Yoshikawa, Y., Baba, Y., Mizutani, H., Kubo, T., Shimoda, C., 2018. Observed Features of Langmuir Turbulence Forced by Misaligned Wind and Waves under Destabilizing Buoyancy Flux. J. Phys. Oceanogr. 48, 2737–2759. https://doi.org/10.1175/JPO-D-18-0038.1

Zheng, Y., Shinoda, T., Lin, J.-L., Kiladis, G.N., 2011. Sea Surface Temperature Biases under the Stratus Cloud Deck in the Southeast Pacific Ocean in 19 IPCC AR4 Coupled General Circulation Models. J. Clim. 24, 4139–4164. https://doi.org/10.1175/2011JCLI4172.1

Zippel, S.F., Farrar, J.T., Zappa, C.J., Miller, U., Laurent, L.S., Ijichi, T., Weller, R.A., McRaven, L., Nylund, S., Bel, D.L., 2021. Moored Turbulence Measurements Using Pulse-Coherent Doppler Sonar. J. Atmospheric Ocean. Technol. 38, 1621–1639. https://doi.org/10.1175/JTECH-D-21-0005.1

Zuidema, P., Chang, P., Medeiros, B., Kirtman, B.P., Mechoso, R., Schneider, E.K., Toniazzo, T., Richter, I., Small, R.J., Bellomo, K., Brandt, P., Szoeke, S. de, Farrar, J.T., Jung, E., Kato, S., Li, M., Patricola, C., Wang, Z., Wood, R., Xu, Z., 2016. Challenges and Prospects for Reducing Coupled Climate Model SST Biases in the Eastern Tropical Atlantic and Pacific Oceans: The U.S. CLIVAR Eastern Tropical Oceans Synthesis Working Group. Bull. Am. Meteorol. Soc. 97, 2305–2328. https://doi.org/10.1175/BAMS-D-15-00274.1